

Enabling Robust Radar-based Localization and Vital Signs Monitoring in Multipath Propagation Environments

Mercuri, Marco; Lu, Yiting ; Polito, Salvatore ; Wieringa, Fokko ; van der Veen, Alle-Jan; Van Hoof, Chris; Torfs, Tom

DOI

[10.1109/TBME.2021.3066876](https://doi.org/10.1109/TBME.2021.3066876)

Publication date

2021

Document Version

Final published version

Published in

IEEE Transactions on Biomedical Engineering

Citation (APA)

Mercuri, M., Lu, Y., Polito, S., Wieringa, F., van der Veen, A.-J., Van Hoof, C., & Torfs, T. (2021). Enabling Robust Radar-based Localization and Vital Signs Monitoring in Multipath Propagation Environments. *IEEE Transactions on Biomedical Engineering*, 68(11), 3228 - 3240. <https://doi.org/10.1109/TBME.2021.3066876>

Important note

To cite this publication, please use the final published version (if applicable). Please check the document version above.

Copyright

Other than for strictly personal use, it is not permitted to download, forward or distribute the text or part of it, without the consent of the author(s) and/or copyright holder(s), unless the work is under an open content license such as Creative Commons.

Takedown policy

Please contact us and provide details if you believe this document breaches copyrights. We will remove access to the work immediately and investigate your claim.







Green Open Access added to TU Delft Institutional Repository

'You share, we take care!' - Taverne project

<https://www.openaccess.nl/en/you-share-we-take-care>

Otherwise as indicated in the copyright section: the publisher is the copyright holder of this work and the author uses the Dutch legislation to make this work public.

Enabling Robust Radar-Based Localization and Vital Signs Monitoring in Multipath Propagation Environments

Marco Mercuri , Yiting Lu , Salvatore Polito, Fokko Wieringa, Yao-Hong Liu , *Senior Member, IEEE*, Alle-Jan van der Veen , *Fellow, IEEE*, Chris Van Hoof , *Member, IEEE*, and Tom Torfs 

Abstract—Objective: Over the last two decades, radar-based contactless monitoring of vital signs (heartbeat and respiration rate) has raised increasing interest as an emerging and added value to health care. However, until now, the flaws caused by indoor multipath propagation formed a fundamental hurdle for the adoption of such technology in practical healthcare applications where reliability and robustness are crucial. Multipath reflections, originated from one person, combine with the direct signals and multipaths of other people and stationary objects, thus jeopardizing individual vital signs extraction and localization. This work focuses on tackling indoor multipath propagation. **Methods:** We describe a methodology, based on accurate models of the indoor multipaths and of the radar signals, that enables separating the undesired multipaths from desired signals of multiple individuals, removing a key obstacle to real-world contactless vital signs monitoring and localization. **Results:** We also demonstrated it by accurately measure individual heart rates, respiration rates, and absolute distances (range information) of paired volunteers in a challenging real-world office setting. **Conclusion:** The approach, validated using a frequency-modulated continuous wave (FMCW) radar, was shown to function in an indoor environment where radar signals are severely affected by multipath reflections. **Significance:** Practical applications arise for health care, assisted living, geriatric and quarantine medicine, rescue and security purposes.

Index Terms—Array signal model, biomedical applications, contactless, doppler, frequency-modulated continuous wave, localization, multipath, remote radar sensing, single-input and single-output radar, vital signs monitoring.

I. INTRODUCTION

RADAR technologies represent an emerging, increasingly investigated modality in health care, with likely benefits for the elderly population, healthcare professionals, and economy [1]–[4]. The primary application is remote monitoring of vital signs, in particular heartbeat and respiration rate. The largest attractiveness of radar-based vital sign monitoring is that it can be done remotely. This has aroused an increasing interest especially where wearable medical devices cannot be used (e.g., patients with severe and extensive burn wounds) or create discomfort and are unpleasant for long-term use (e.g., while sleeping). To maximally utilize its capability, the goal is to enable people maximal freedom to move around without restrictions, while tracking their positions and measuring their vital signs. Performing concurrently the two operations allows to correctly assign the cardiopulmonary values to the subjects, who are identified by their positions (this does not rise privacy concerns). This enables the use of this technology in many medical applications of strong interest. Some examples are: sleep monitoring; offering night nurses in low-care wards an overview whether all patients are in bed and doing well; contactless monitoring of patients in multi-bed rooms, recovering their ability for ambulant walking (even just visiting the toilet unaided is a major step forward) as well as elderly or handicapped people living with assistance-on-call; monitoring elderly people in nursing home. Radars can even detect subtle changes over time in vital signs that are not obvious in a one-off visit by a doctor. This technology is also ideal in situations with risk of infection or pandemics (e.g., COVID-19 crisis) to remotely monitor household members in quarantine or in hospitals (e.g., departments of infectious diseases) to reduce contamination risks. Moreover, for prolonged monitoring in the home setting, daily patterns in locations and vital signs also offer objective insights in general fitness level over time, without the obtrusive privacy aspects. Radars can be used in other fields even beyond medical, such as ambient light and temperature smart control, driver monitoring, surveillance, and for search

Manuscript received November 27, 2020; revised January 6, 2021 and February 15, 2021; accepted March 15, 2021. Date of publication March 17, 2021; date of current version October 20, 2021. (Corresponding author: Marco Mercuri.)

Marco Mercuri is with imec – Netherlands, 5656 AE Eindhoven, The Netherlands (e-mail: Marco.Mercuri@imec-nl.nl).

Yiting Lu is with imec – Netherlands, 5656 AE Eindhoven, The Netherlands, and also with NXP Semiconductors, The Netherlands.

Salvatore Polito and Yao-Hong Liu are with the imec – Netherlands, The Netherlands.

Fokko Wieringa is with imec – Netherlands, The Netherlands, and also with Maastricht University, The Netherlands.

Alle-Jan van der Veen is with TU Delft, Department of Microelectronics, The Netherlands.

Chris Van Hoof is with imec – Netherlands, The Netherlands, with imec - OnePlanet Research Center, The Netherlands, with imec, Belgium, and also with KU Leuven, Belgium (e-mail: Chris.VanHoof@imec.be).

Tom Torfs is with imec, Belgium.

Digital Object Identifier 10.1109/TBME.2021.3066876

and rescue situations to detect people in smoke-filled areas or underneath collapsed buildings [5]–[8].

However, the biggest challenge in indoor environments is to detect the sub-millimetre motion on the chest surface caused by the cardiopulmonary activity in order to properly locate multiple subjects and to accurately monitor their vital signs. In fact, an inherent problem is the severe multipath effect [9]–[11], which jeopardizes the monitoring of multiple subjects. Multipath occurs when a signal takes two or more paths from the transmitting antenna to the receiving antenna and depends on the room structure and on the presence of objects (including those behind radar-transparent walls). As a consequence, even moving a small object in the environment changes the multipath reflections. To be clinically meaningful, radar technologies should be flexible to work in all practical circumstances that can reasonably be expected. In indoor environments, it will commonly occur that a multipath component from one person has an identical delay (i.e., time of flight) as the direct path signal for another person. For a straight-forward radar system, these signals then would seem to originate from the same range bin (i.e., location), resulting in non-linear combinations of the Doppler signals (i.e., phase shifts) generated by the subjects, hence causing false localizations and incorrect vital signs extraction. The situation gets even more problematic in presence of static reflectors (i.e., clutter, objects). In fact, the multipath reflections of a subject can have an identical delay (i.e., time of flight) as the direct path signal of a stationary object. Intuitively, this can be interpreted as a Doppler signature (radar ghost) originating in the range bin where the stationary object is present. Therefore, static objects cannot be simply treated as stationary in real-world situations where multipath is present.

Until now, indoor multipath effects were insufficiently addressed. In the current state-of-the-art, pure continuous wave (CW) radars have been extensively used to monitor the vital signs of a single individual [7], [12]–[22]. Due to their narrowband nature, pure CW-architectures are neither able to determine absolute distances nor to separate reflections temporally. This means that they cannot monitor multiple subjects and their detection sensitivity is strongly influenced by static reflectors and multipaths. Some of these limitations can be solved by ultra-wideband (UWB) technology, that employs a wide bandwidth (typically defined as greater than 20% of the center frequency or 500 MHz). In this category falls the FMCW, stepped-frequency continuous wave (SFCW), phase-modulated continuous wave (PMCW) and UWB impulse-radio (UWB-IR) radars. For trade-offs between UWB radars, we refer the reader to [23]. These architectures have been demonstrated to locate multiple persons and monitor their vital signs but only under the strong restriction that the signals coming from different individuals do not interfere with each other, so that the subjects can be treated independently and therefore ignoring multipath effects [24]–[45]. This assumption can be achieved during controlled lab experiments through one or more of the following conditions: (1) using highly directive antennas (e.g., beamforming, horn antennas); (2) sufficiently separating the targets in the angular dimension (i.e., the signals coming from different individuals hardly interfere with each other); (3) with no objects in the line of sight between the radar

and the person, or placed strategically to avoid generation of significant interferences (i.e., the reflection from the human body is always the strongest one); (4) removing any metal and highly reflective objects from the scene. Clearly, those conditions form limitations that preclude universal application in real life situations. Techniques like classic Doppler phase extraction [37], blind source separation (BSS) [22], complex signal demodulation [12], arctangent demodulation [13] and linear demodulation [31] have been investigated to retrieve the vital signs parameters, however they are all based on the single target or on the independent multi-targets restrictions. Using these techniques, in most of the current state-of-the-art works, vital signs extraction is performed after a prior knowledge of the position(s) of the subject(s), namely the Doppler information is extracted from the known range bin(s) where the person(s) is (are) present (i.e., manual localization). Some solutions have been also proposed for automatic target localization based on vital signs [35], [37]. Those approaches rely on the variation of the range spectrum to differentiate humans from stationary targets. The idea is that the physiological movements, over an interval of time of a few seconds, involve a larger standard deviation (std) than static objects. Therefore, the range bins with large variations indicate the location of human targets (i.e., std-based localization). In any case, current state-of-the-art algorithms require a priori knowledge of the number of subjects to be monitored. In practical situations, this information is often not available. The aforementioned techniques and approaches fail in presence of multipaths, which are always present in real-world environments and practical situations, resulting in ghost signals, appearing both in copies of the same target at different distances and in new (therefore false) targets originated by the combinations of direct paths and multipaths. A distinction needs to be made between single target and multi-target scenarios. In the first case, with pure CW architectures, the signals from the subject and his/her copies combine together generating an overall distorted Doppler signal. In the second case, with UWB architectures, influenced by the presence of clutter, it is common that the quality of the vital signs signal from a copy is scaled as higher than the true signal of the pertaining person, causing location of a subject in a wrong position. In case of multiple targets, and relevant only for UWB architectures, the multipaths caused by one person combine with the reflected signals from other persons and from static objects, generating new Doppler signals (i.e., radar ghosts) thereby jeopardizing both vital signs extraction as well as localization.

We propose and demonstrate a methodology, based on a compact single-input and single-output (SISO) FMCW radar and on an indoor radar signal model, which is able to separate the undesired contributions of multipaths and static reflectors from the desired signals of each single individual, thereby enabling accurate simultaneous one-dimensional (1-D) location (i.e., absolute distance) and vital signs monitoring of multiple persons, even in case of (partial) occlusion by static objects such as desks or chairs and through radio-transparent physical barriers such as windows. Moreover, the proposed algorithm determines autonomously the number of people present in the monitored environment.

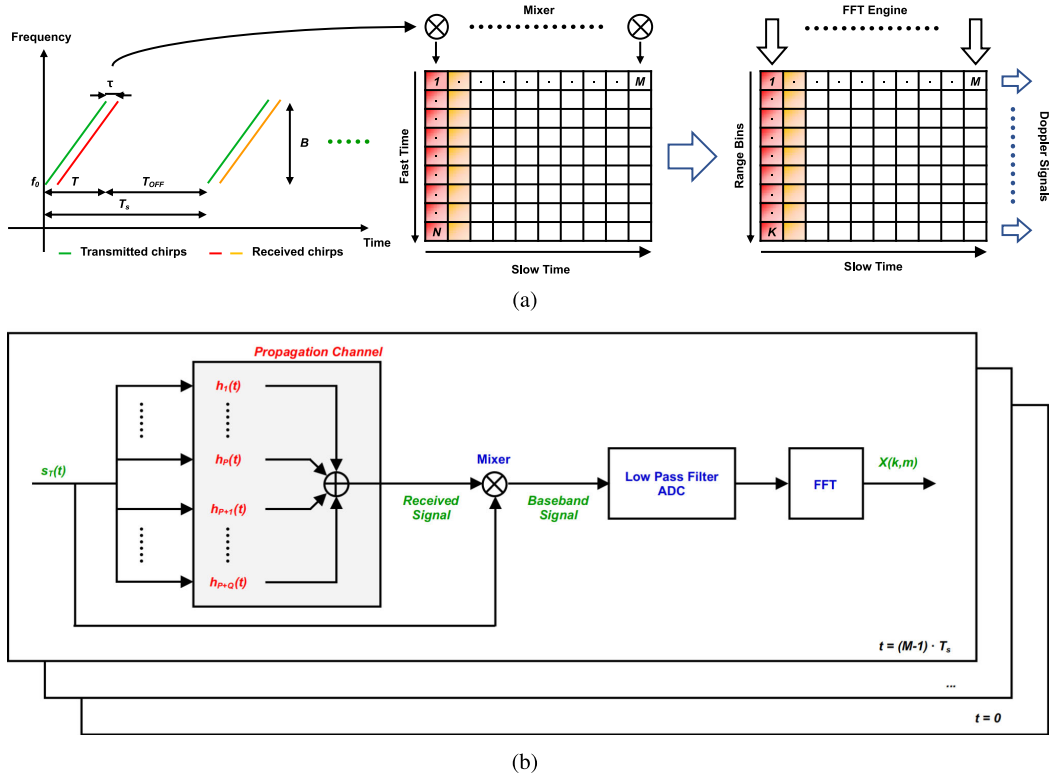


Fig. 1. Data model. (a) Graphical illustration of the generation of the data model matrix from consecutive FMCW signals. (b) Block diagram of the data model.

The remainder of this article is organized as follows. In Section II, the array signal model is derived. In Section III, the radar proposed methodology is presented and detailed. In Section IV, the radar sensor is described. Experimental results conducted on human volunteers are shown in Section V.

II. ARRAY SIGNAL MODEL

A. SISO FMCW Data Matrix

A linear FMCW radar transmits a series of signals, called *chirps*, whose instantaneous frequency linearly increases over time (Fig. 1(a)). Each chirp is T seconds long and it is transmitted with a certain repetition interval T_s . Between two consecutive *chirps*, no signal is transmitted during $T_{OFF} = T_s - T$. The interval τ is the round-trip delay that the FMCW signal takes to reach the target and to be reflected back to the receiver. The baseband signals (called *beat signals*), resulting from mixing the copies of the transmitted *chirps* with the received *chirps*, are digitized and arranged in a $N \times M$ data matrix, where N is the number of samples acquired per beat signal and depends both on T and on the sampling time T_f of the analog-to-digital converter (ADC) while M is the number of beat signals that are used in the data processing, collected each T_s . In radar terminology, T_f determines the fast time while T_s determines the slow time (Fig. 1(a)). This matrix is preprocessed by applying the Fast Fourier Transform (FFT) per column. This creates a $K \times M$ complex data matrix, whose elements are denoted by $X(k,m)$, with $k = 0, \dots, K-1$ being the range bin index, $K = N$, and $m = 0, \dots, M-1$ is the index in slow time. The M columns contain the

range profiles, determined each T_s , while the K rows contain the Doppler signals (i.e., phase shifts containing vital signs information) from the range bins. The mathematical formulation of $X(k,m)$ is derived in Subsection II-C including also the effect of the multipath.

B. Direct Path and Multipath Combination

Let's consider a scenario with two stationary and normally breathing subjects in two different range bins (i.e. two different distances) in a room: Subject 1 is in range bin 1 while Subject 2 is in range bin 2. We neglect, in this explanation, the effects of static reflectors and we consider only range bin 1 and 2. The slow-time signals $s(t)$ resulting from the direct paths of the two subjects can be expressed as:

$$s_1(t) = A_1(t)e^{j\phi_1(t)}, \quad (1)$$

$$s_2(t) = A_2(t)e^{j\phi_2(t)}, \quad (2)$$

where the subscripts 1 and 2 indicate respectively Subject 1 (the closest to the radar) and Subject 2 (the farther to the radar), $A(t)$ is the amplitude non-linearly modulated by the chest motion, and $\phi(t)$ is the Doppler shift, namely the vital signs information we are interested to retrieve. Let's assume a typical indoor situation where a multipath of the Subject 1 combines with the direct path of the farther Subject 2. This can be intuitively interpreted as the multipath caused by Subject 1 comes from range bin 2. Mathematically this can be expressed with a total slow-time signals $s_{bin2}(t)$:

$$s_{bin2}(t) = \alpha A_1(t)e^{j[\phi_1(t)+\theta]} + A_2(t)e^{j\phi_2(t)}, \quad (3)$$

where α and θ are used to model respectively the attenuation and the fixed phase shift on the multipath compared to the corresponding direct path. Knowing range bin 1, using current UWB state-of-the-art approaches [24]–[40], it is highly likely to retrieve the vital signs information $\phi_1(t)$ of Subject 1. This because UWB technologies can separate temporally the reflections and we are assuming in this explanation that *range bin 1* is not influenced by the presence of Subject 2 who is behind Subject 1 (in reality there is always the spreading effect of the FFT). This does not hold for CW radars [7], [12]–[22] which can monitor only one single person and the detection sensitivity is strongly influenced by the multipaths of the same target. However, the big challenge is to retrieve the vital signs information of Subject 2 $\phi_2(t)$. In fact, since we are interested in the phase information (i.e., Doppler signal), (3) shows a non-linear combination of the Doppler signals (i.e., phase information). For example, let's consider a typical indoor situation where the multipath is stronger in magnitude than the direct path, i.e., $\alpha A_1(t) \gg A_2(t)$. Under this condition, (3) can be approximated as [21]:

$$s_{bin2}(t) \approx A_T(t)e^{j\left\{\left[\phi_1(t)+\theta\right]+\frac{A_2(t)}{\alpha A_1(t)}\sin\left[\phi_2(t)-\phi_1(t)-\theta\right]\right\}}, \quad (4)$$

where $A_T(t)$ is the overall magnitude. As it is possible to note, $\phi_2(t)$ is non-linearly combined in the exponential argument and it is also multiplied by $A(t)/\alpha A_1(t) \ll 1$. Current state-of-the-art approaches fail to extract $\phi_2(t)$ as they rely on the assumption that the subjects' reflections do not interfere each other hence they can be treated independently. However, (3) and (4) mathematically demonstrate that this assumption is not valid in severe multipath conditions. In addition, the situation is even more complicated when there is no information on the subjects' location and when we consider the effects of the static reflectors and all the range bins (in this discussion we considered only two range bins). Non-linear signal combinations are in fact affecting all the range bins.

With the proposed methodology, detailed in Section III, we are able to isolate the single independent sources $s_1(t)$ and $s_2(t)$ from which we can extract accurately $\phi_1(t)$ and $\phi_2(t)$.

C. Multipath Propagation Model

We adopted the multipath channel model proposed by Jakes [46] which includes the essential propagation parameters, namely magnitude, frequency and phase. Based on the limited room size, we consider only the first L range bins of the K total available ones. Within a range bin, differences in delays are small and translate into phase shifts. Correspondingly, we assume that the number of possible path delays is also L . As a result, the (slowly time-varying) multipath propagation channel impulse response $h(t, m)$ is modelled as:

$$h(t, m) = \sum_{l=0}^{L-1} \beta_l \cdot \delta(t - \tau_l(m)), \quad (5)$$

where $\delta(\cdot)$ is the Dirac delta function, l is the path index, τ is the propagation of the l -th path, and β_l is the complex path gain which indicates the overall attenuation and phase shift. We assume that there are P people and Q static clutter in

the room, which are regarded as point scatters and, therefore, the summation of all reflections from each infinitesimal point of a target's surface which falls into the same range bin can be regarded as one overall reflection through one propagation path (the validity of this assumption was already demonstrated through simulations and experiments in literature [12]). The only difference between the two types of targets is that the subjects have physiological activities (i.e., variable phase in slow time or Doppler signal), leading to a time varying $\tau_l(m)$, while the static clutter involves a constant τ_l (i.e., constant phase in slow time or Doppler signal).

The received signal $s_R(t, m)$ over a multipath channel can be modelled as the convolution between the channel impulse response $h(t, m)$ and the transmitted signal $s_T(t, m)$. It can be expressed as:

$$\begin{aligned} s_R(t, m) &= \sum_{i=0} s_T(t, m) * h(t, m) = \\ &= \sum_{i=0} \sum_{l=0} \beta_{i,l} \cdot s_T(t - \tau_{i,l}(m)), \end{aligned} \quad (6)$$

with

$$s_T(t, m) = a_T e^{j2\pi \int_0^t (f_0 + \rho t) dt} = a_T e^{j2\pi \left(f_0 + \frac{\rho}{2} t\right) t}, \quad (7)$$

$$\tau_{i,l}(m) = \begin{cases} 2 \frac{d_{i,l} + y_i(m)}{c_0} & \text{for human target} \\ 2 \frac{d_{i,l}}{c_0} & \text{for clutter/object} \end{cases}, \quad (8)$$

where $*$ is the convolution operator, a_T is the complex amplitude indicating the amplitude of the chirp and its initial phase, $\rho = B/T$ is the sweeping rate, m is the slow time index, i is the index corresponding to the i -th target/object, l is the path index, d is the path distance, $y(m)$ is the chest surface displacement and it is the parameter of interest, and c_0 is the speed of light. The baseband signal $s_B(t, m)$, obtained by matched filtering the received signal with the transmitted signal, can be modelled as:

$$\begin{aligned} s_B(t, m) &= s_T(t, m) \cdot s_R^*(t, m) = \\ &= \sum_{i=0} \sum_{l=0} \beta_{i,l}^* a_T^2 e^{j2\pi \left(f_0 \tau_{i,l}(m) - \frac{\rho}{2} \tau_{i,l}^2(m) + \rho \tau_{i,l}(m) t\right)} \approx \\ &\approx \sum_{i=0} \sum_{l=0} \beta_{i,l}^* a_T^2 e^{j2\pi f_0 \tau_{i,l}(m)} \cdot e^{j2\pi \rho \tau_{i,l}(m) t}, \end{aligned} \quad (9)$$

where the superscript $*$ indicates the complex conjugate operation. We neglected the quadratic term because $\tau_{i,l}(m)$ is close to zero. The digitized baseband signal can be expressed as:

$$s_B(n, m) \approx \sum_{i=0} \sum_{l=0} \beta_{i,l}^* a_T^2 e^{j2\pi f_0 \tau_{i,l}(m)} \cdot e^{j2\pi \rho \tau_{i,l}(m) n T_f}, \quad (10)$$

where n is the fast time index and T_f is the fast time sampling time (i.e., ADC sampling rate). After performing the FFT in fast time, the frequency domain signal $X(k, m)$ becomes:

$$X(k, m) = \mathcal{F} \{s_B(n, m) \cdot w(n)\}$$

$$\begin{aligned}
&= \sum_{i=0} \sum_{l=0} e^{j2\pi f_0 \tau_{i,l}(m)} \cdot W\left(\frac{2\pi k}{K} - 2\pi \rho \tau_{i,l}(m)\right) \\
&\approx \sum_{i=0} \sum_{l=0} e^{j2\pi f_0 \tau_{i,l}(m)} \cdot W(k), \quad (11)
\end{aligned}$$

with

$$W(k) = W\left(\frac{2\pi k}{K} - 2\pi \rho \tau_{i,l}(m)\right), \quad (12)$$

where \mathcal{F} is the fast Fourier transform operator, $w(n)$ is a rectangular window function in fast time, $w(n)$ and $W(k)$ are a Fourier pair. Since the rectangular window in frequency domain is a sinc function with gradients close to zero around $2\pi \rho \tau_{i,l}$, the frequency domain window function $W_{i,j}(k)$ can be considered as a fixed one in slow time. A sketch of this data model is shown in Fig. 1 b. Assuming P subjects and Q static clutter in a room, (11) can be rewritten as:

$$X(k, m) = \sum_{i=1}^P a_i(k) e^{j\phi_i(m)} + c(k), \quad (13)$$

with

$$a_i(k) = \sum_l e^{j\frac{4\pi f_0 d_{i,l}}{c_0}} \cdot \beta_{i,l}^* a_T^2 W_{i,l}(k), \quad (14)$$

$$c(k) = \sum_{i=P+1}^{P+Q} \sum_l e^{j\frac{4\pi f_0 d_{i,l}}{c_0}} \cdot \beta_{i,l}^* a_T^2 W_{i,l}(k), \quad (15)$$

$$\phi_i(m) = \frac{4\pi f_0}{c_0} y_i(m), \quad (16)$$

where $\phi_i(m)$ is the Doppler shift caused by the vital signs on the FMCW signal. The observation signal $X(k, m)$ is a dual variable function of k and m and forms a two-dimensional observation matrix \mathbf{X} with factorization

$$\mathbf{X} = \mathbf{H}\mathbf{S} + \mathbf{C}, \quad (17)$$

where

$$\mathbf{H} = \begin{bmatrix} a_1(0) & \cdots & a_p(0) \\ \vdots & \ddots & \vdots \\ a_1(L-1) & \cdots & a_p(L-1) \end{bmatrix} \quad (18)$$

is an $L \times P$ complex mixing matrix derived from (5),

$$\mathbf{S} = \begin{bmatrix} e^{j\phi_1(0)} & e^{j\phi_1(1)} & \cdots & e^{j\phi_1(M-1)} \\ \vdots & \vdots & \ddots & \vdots \\ e^{j\phi_P(0)} & e^{j\phi_P(1)} & \cdots & e^{j\phi_P(M-1)} \end{bmatrix} \quad (19)$$

is a $P \times M$ complex matrix containing the Doppler shifts (i.e., vital signs information) caused by the P subjects at each T_s , and

$$\mathbf{C} = \begin{bmatrix} c(0) & \cdots & c(L-1) \end{bmatrix}^T \cdot \mathbf{1}^T \quad (20)$$

is an $L \times M$ matrix with identical columns containing the direct current (DC) information in slow-time resulting from static reflections where the superscript T indicates the transpose. Here

$\mathbf{1}$ is a length M all-ones column vector. In presence of additive noise, the data model becomes as

$$\mathbf{X} = \mathbf{H}\mathbf{S} + \mathbf{C} + \mathbf{N}, \quad (21)$$

where \mathbf{N} is an $L \times M$ matrix containing zero mean additive noise. The next step is to perform alternate current (AC) coupling to (21) in order to remove the DC components (i.e., the mean values) while still preserving the physiological (i.e., variable) motions. This is achieved removing \mathbf{C} in \mathbf{X} using a projection (or centering matrix) \mathbf{P} such that $\mathbf{C}\mathbf{P} = \mathbf{0}$. This requires $\mathbf{1}^T \mathbf{P} = \mathbf{0}$, where $\mathbf{1}$ is a vector with all entries equal to 1, so that

$$\mathbf{P} = \mathbf{I} - \mathbf{1}(\mathbf{1}^T \mathbf{1})^{-1} \mathbf{1}^T, \quad (22)$$

where \mathbf{I} is an identity matrix. The result is:

$$\mathbf{X}\mathbf{P} = \mathbf{H}\mathbf{S}\mathbf{P} + \mathbf{C}\mathbf{P} + \mathbf{N}\mathbf{P} = \mathbf{H}\mathbf{S}\mathbf{P} + \mathbf{N}\mathbf{P}. \quad (23)$$

Considering

$$\bar{\mathbf{X}} = \mathbf{X}\mathbf{P}, \quad (24)$$

$$\bar{\mathbf{S}} = \mathbf{S}\mathbf{P}, \quad (25)$$

$$\bar{\mathbf{N}} = \mathbf{N}\mathbf{P}, \quad (26)$$

(23) becomes

$$\bar{\mathbf{X}} = \mathbf{H}\bar{\mathbf{S}} + \bar{\mathbf{N}}. \quad (27)$$

The statistic properties of this data model are:

- 1) $\bar{\mathbf{S}}$ has full rank P ;
- 2) each row of $\bar{\mathbf{S}}$ is regarded as an independent and zero mean source. All the signals are assumed to be random, independent, and identically distributed;
- 3) the noise is assumed to be additive, white, zero mean, complex Gaussian distributed, and independent from the sources.

The model of (27) serves as starting point for the combined vital-sign monitoring and automatic localization algorithm described in the next Section. Although it was derived for an FMCW radar, (17)-(27) are generic for any UWB architecture.

III. METHODS

The block diagram of the algorithm is shown in Fig. 2. With the support of Fig. 3, we explain the proposed methodology. Fig. 3 a shows the In-phase and Quadrature (IQ) signals, namely the real and imaginary components, of the Doppler signal in each range bin for a measurement with two subjects, seated on chairs and behind desks, whose chest surfaces were respectively at 1.07 m and 2.26 m distance from the radar. The experiment was conducted in the environment (Fig. 3 b), mimicking an educational class setting, where we validated the proposed approach and system (details in Section V). In an ideal situation and with a range resolution of 20 cm, we would expect only Doppler information in range bins 6 and 11 (for respectively Subject 1 and Subject 2). However, as it can be seen in Fig. 3 a, each range bin contains signals which can be direct paths, multipaths, or combinations of them. Their amplitudes provide information of the impact of multipath in the considered scenarios. We observe: (1) the IQ components present very similar amplitudes and

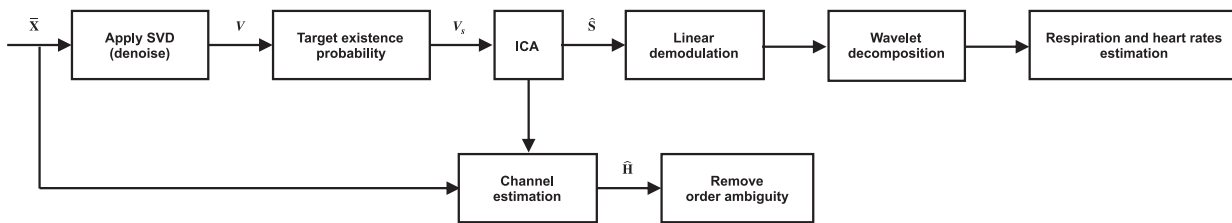


Fig. 2. Block diagram of the vital-sign monitoring and localization algorithms.

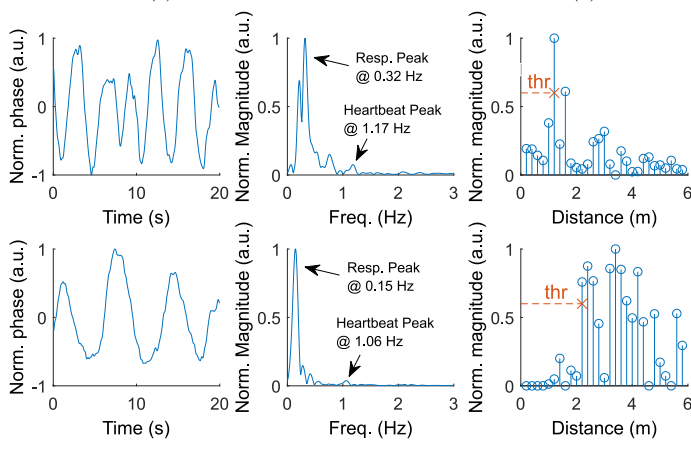
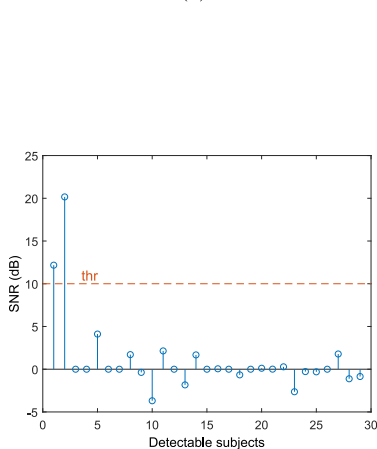
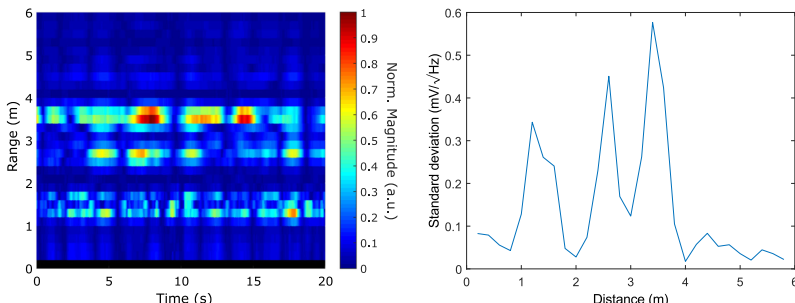
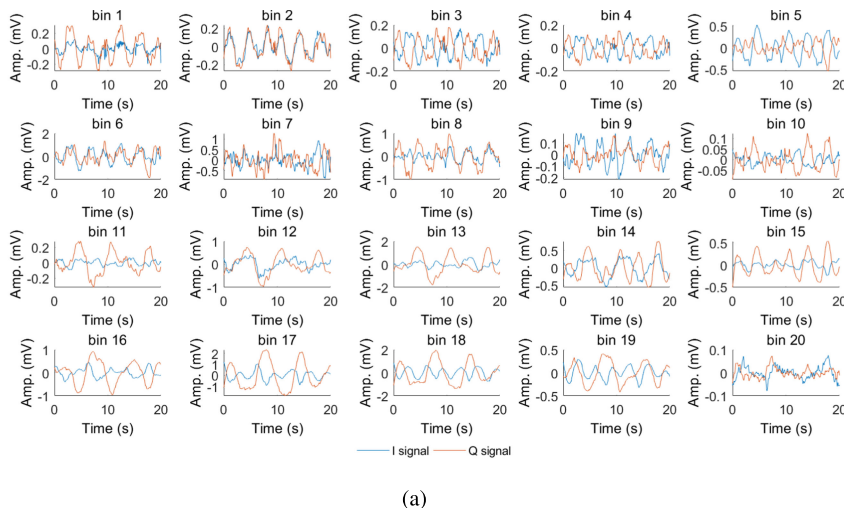


Fig. 3. Vital-sign monitoring and localization algorithm example. (a) IQ signals extracted from the first 20 range bins. From these signals, obtained after applying the FFT to the $K \times M$ matrix, it is possible to determine the Doppler information. (b) Experiment with two subjects respectively at about 1 m and about 2 m distance from the radar. The experimental environment mimics an educational class setting. (c) Range profile. (d) Standard deviation profile obtained from the $K \times M$ matrix processed with the FFT. (e) Target existence probability. (f) Vital signs signals (left), relative spectra (middle) and channel responses (right) of Subject 1 (top plots) and Subject 2 (bottom plots) determined using the proposed methodology.

trends in many of the range bins, raising the question: “how many targets are truly present?”; (2) radar ghosts are generated, i.e., the radar detects non existing people or represents a lifeless object as alive. More precisely, a simple visual check clearly reveals that the signals in bin 6 (which can be approximated as 6 periods of a sinewave in 20 seconds) are also fairly replicated with different amplitudes and initial phases in bins 1-5,8-10,14,15,17-19. Range bins 1 to 5 show very small IQ components. Since the multipath cannot influence the range bins before the target itself, the IQ signals in those range bins are entirely due to FFT spreading. Range bins 8,14,15,17-19 show IQ signals whose amplitudes are stronger than the ones of range bins 1-5. These contributions are mainly due to multipath effects. In fact, the FFT spreading effect cannot result in amplitudes higher than the ones reported in range bins 1-5 and should decrease with the distance from the range bin where the target is (we use a window function before performing the FFT). Similar considerations apply for the signals of bin 11 (which can be considered as 3 periods of a sinewave in 20 seconds), which are replicated in bins 12-14,16-19. In addition, the two subjects interfere with each other in bins 14,17-19 where the I signal corresponds to one subject while the Q signal corresponds to the other subject. The range profile of this experiment is depicted in Fig. 3 c. It is possible to see strong responses within 2.6 m and 3.4 m where there were no targets. This is indeed a consequence of the multipath. We can see the response of Subject 1 at 1.2 m. Obviously, the first target cannot be affected by multipath but its response is strongly affected by the wide desk placed in front of it which causes considerable spreading of the transmitted and reflected signals. On the other hands, there is no response of Subject 2 at 2.2 m. The std-based localization approach [35], [37] fails in presence of multipaths. This is demonstrated by the std profile depicted in Fig. 3 d, where the two highest peaks are respectively at 2.6 m (bin 13) and 3.4 m (bin 17), resulting in wrong localizations. Actually, in this case, it looks more probable to conclude that there are 3 persons. As expected, this is in line with the range profile of Fig. 3 c. Looking at bin 13 in Fig. 3 a, it appears that it contains the signals originated from Subject 2 (i.e., 3 periods of a sinewave in 20 seconds). In this bin, the std response is higher than the one retrieved from the direct signal originated from the chest surface of Subject 2 at bin 11. This is a normal result in real measurement condition: the chest surface, containing both respiratory and heartbeat information, involves a smaller vibration than the one due to the abdomen which, depending on the radar positioning, can fall in adjacent bins and it does not contain heartbeat information. Bin 17, instead, results from the combination of two targets (I signal is mainly generated by Subject 2 while Q signal by Subject 1). In this bin, we report the highest std response. This is expected when multipaths (especially if generated by abdomen area) combine coherently.

With the proposed algorithm, we aim at isolating the single independent sources $\bar{\mathbf{S}}$ from which we can extract accurately the relative Doppler signals in order to first determine the number of targets and then to estimate their vital signs and absolute distances (i.e., range information). The first step is to reduce the noise by applying the singular value decomposition (SVD) to $\bar{\mathbf{X}}$.

The result is used to determine the number of persons P (*target existence probability*) in the monitored environment. We specify that in real environments P cannot be determined by simply calculating the rank of $\bar{\mathbf{X}}$. Once knowing the number of targets, the SVD result is further processed by an independent component analysis (ICA) algorithm in order to estimate the sources $\hat{\mathbf{S}}$. The vital signs information is preserved in the phase information of $\hat{\mathbf{S}}$. The AC coupling step used to obtain (27) removes all the DC information of the target, resulting in a distortion in the phase (angle) extraction [12], [31]. Therefore, we used the linear demodulation algorithm on $\hat{\mathbf{S}}$ to perform phase demodulation in order to extract the vital signs information $\hat{y}(m)$. At this point, we face an ordering ambiguity issue: we are still not able to indicate which source (i.e., vital signs signal) corresponds to which subject. From (27), \mathbf{H} determines the linear combinations of the sources in $\bar{\mathbf{S}}$, so the magnitudes of the elements in \mathbf{H} indicate the energy of the sources in every range bin. From the observation matrix $\bar{\mathbf{X}}$ and the estimated source matrix $\hat{\mathbf{S}}$, we can estimate $\hat{\mathbf{H}}$. Knowing the propagation channels \mathbf{H} of the sources, we can 1-D localize the targets and remove the ordering ambiguity.

Fig. 3 e shows the estimated target existence probability in terms of signal-to-noise ratio (SNR) of the uncorrelated sources obtained after the SVD. Fixing a threshold *thr* (dashed line in Fig. 3 e), from the stem plots it clearly appears that there are two subjects in the monitored environment. Fig. 3 f shows the extracted vital signs, the resulting spectra, and the corresponding channel responses from which the targets can be correctly 1-D located. In the channel responses, the outliers originating from additive noise are small and can easily be excluded by applying a threshold (dashed line in Fig. 3 f), while the outliers resulting from multipaths can be removed by detecting the shortest direct path (\times in Fig. 3 f). The spectral plots indicate the vital signs rates. They are in fair agreement with the reference values: the respiration and heart rates of Subject 1 were 0.32 Hz and 1.19 Hz, while for Subject 2 they were respectively 0.15 Hz and 1.06 Hz. In this example, for Subject 1, the estimated heart rate and the corresponding reference rate differ 0.02 Hz (corresponding to 1.2 beats/min) which is a clinically acceptable difference [47]. The respiration and heartbeat signals can be obtained by filtering properly the vital signs signals. In doing so, in the experimental validation of this work (details in Section V), we used the Wavelet decomposition (we chose the Discrete Meyer mother wavelet) and the corresponding rates were estimated through FFT.

A. Singular Value Decomposition

We reduce the noise by applying SVD to (27) as:

$$\begin{aligned} \bar{\mathbf{X}} &= \mathbf{H}\bar{\mathbf{S}} + \mathbf{N} = \mathbf{U} \cdot \boldsymbol{\Sigma} \cdot \mathbf{V}^{\mathbf{H}} = \\ &= \begin{bmatrix} \mathbf{U}_s & \mathbf{U}_n \end{bmatrix} \begin{bmatrix} \boldsymbol{\Sigma}_s & 0 \\ 0 & \boldsymbol{\Sigma}_n \\ 0 & 0 \end{bmatrix} \begin{bmatrix} \mathbf{V}_s^{\mathbf{H}} \\ \mathbf{V}_n^{\mathbf{H}} \end{bmatrix}, \end{aligned} \quad (28)$$

where \mathbf{U} is an $L \times L$ unitary matrix containing left singular vectors, \mathbf{V} is an $M \times M$ unitary matrix containing right singular

vectors and its superscript indicates the Hermitian transpose, and Σ is a diagonal matrix containing all the singular values. The first P columns in \mathbf{U} and \mathbf{V} are denoted respectively as \mathbf{U}_s and \mathbf{V}_s , while the remaining columns are denoted as \mathbf{U}_n and \mathbf{V}_n , respectively.

B. Target Existence Probability

In order to estimate P , and therefore to determine \mathbf{V}_s , we calculate the SNR of the uncorrelated sources in \mathbf{V} . A spectrum of a canonical radar-based vital signs signal consists essentially of the respiration fundamental, which is the dominant component of the signal, of one or two decreasing in magnitude respiration harmonics, and of the very small heartbeat fundamental. We consider as *signal power* the power within the fundamental and its first harmonic while the rest of the spectrum is considered as *noise*. The first P sources of \mathbf{V} (i.e., first P columns) produce a high SNR and indicate \mathbf{V}_s while the remaining sources have very low SNR and indicate \mathbf{V}_n . We perform also other checks on the spectrum's local maxima: (1) if the peak, which should indicate the respiration rate, is outside the typical medical ranges, we conclude that this source is noise; (2) we determine the ratio of the strongest peak and its first harmonic. We consider as noise any source producing a ratio less than 2. In those two situations, we fix the SNR to 0 dB. The last operation is to scan the obtained SNR profile starting from the first estimation and stopping when the first descending order uncorrelated source produces an SNR below a threshold which, in this work, was set to 10 dB (this value was determined empirically). The latter source indicates the starting of \mathbf{V}_n while the previous ones are the \mathbf{V}_s sources corresponding to the P subjects.

C. Independent Component Analysis

As noise is assumed to be uncorrelated to the sources in $\bar{\mathbf{S}}$, the columns of \mathbf{V}_s span the same subspace as the rows in $\bar{\mathbf{S}}$ and the columns of \mathbf{V}_n span the noise space. Therefore, \mathbf{V}_s can be expressed as the following linear transform [48]:

$$\mathbf{V}_s^H = \mathbf{A}\bar{\mathbf{S}}, \quad (29)$$

where \mathbf{A} is a $P \times P$ square mixing matrix. Therefore, by taking the signal space, we not only remove the noise falling into the null space, but also pre-whiten the data based on the second order statistic. In (29), the rows of $\bar{\mathbf{S}}$ are the underlying independent sources, \mathbf{A} is a mixing matrix, and the rows of \mathbf{V}_s^H are the mixtures of the sources in $\bar{\mathbf{S}}$. This data model is consistent with the classical cocktail-party problem that can be addressed by the ICA algorithm [49]. Since the first step of ICA, i.e., the pre-whitening, has been done by SVD, the estimation of $\bar{\mathbf{S}}$ only needs one more step, searching for the unmixing matrix \mathbf{W} such that the de-mixed sources have the largest statistical independence [50]:

$$\hat{\mathbf{S}} = \mathbf{W}^H \mathbf{V}_s^H. \quad (30)$$

Based on the central limit theorem, the sum of independent random variables tends to a Gaussian distribution. This gives the inspiration that the estimated independent sources should

tend to be as non-Gaussian distributed as possible. There are various ways to measure non-Gaussianity. One popular criterion is negentropy which is relatively robust and, most importantly, does not require prior knowledge about the probability density functions of the sources [51].

D. Linear Demodulation

Based on the small angle approximation [31], valid for sub-10 GHz radar, a source can be approximated as:

$$s(t) = e^{j\phi(t)} \approx 1 + j\phi(t) - \frac{\phi^2(t)}{2}, \quad (31)$$

where $\phi(t)$ is the phase (Doppler) shift caused by the vital signs. After DC removal, we observe that the imaginary part is more powerful than the real part:

$$\bar{s}(t) \approx j\phi(t). \quad (32)$$

The vital signs information $\hat{y}(t)$ can be extracted applying the linear demodulation [31] to the estimated source $\hat{s}(t)$ and it can be expressed as:

$$\hat{y}(t) = \hat{s}_{LIN}(t) \frac{\lambda_0}{4\pi}, \quad (33)$$

where $\hat{s}_{LIN}(t)$ is the estimated source after the linear demodulation and λ_0 is the wavelength corresponding with the start frequency of the chirp. If the demodulation is performed correctly, (33) is equivalent to the motion of the chest surface $y(t)$ caused by the vital signs. This movement is normally modelled in literature [7], [12]–[40] as the sum of two sinusoidal functions as:

$$y(t) = y_r(t) + y_h(t) = a_r \cos(2\pi f_r t) + a_h \cos(2\pi f_h t), \quad (34)$$

where $y_r(t)$ and $y_h(t)$ indicate respectively the mechanical chest surface displacements caused by respiration (expansion of thorax and lungs) and heart contractions, a_r and a_h are the maximum mechanical displacements caused by the lungs and heart on the chest surface (with typical amplitudes around 4-12 mm and 0.1-0.5 mm [8], respectively), and f_r and f_h are the vital signs frequencies which represent the information to be extracted. Another approach to perform phase demodulation is to use the arctangent demodulation algorithm [13]. We prefer the linear demodulation since is faster and more robust in presence of outliers (e.g., baselines in the Doppler shift, random body movements).

E. Automatic Localization Algorithm

In order to 1-D locate the targets and to remove the order ambiguity, knowing the observation matrix $\bar{\mathbf{H}}$ and the estimated source matrix $\hat{\mathbf{S}}$, we determine $\hat{\mathbf{H}}$ by minimizing the residual error $\|\bar{\mathbf{X}} - \mathbf{H}\hat{\mathbf{S}}\|_2^2$. However, due to the path loss, the observation vectors (rows) in $\bar{\mathbf{X}}$ have unequal power. To better balance the residual errors, we perform a row-wise normalization on $\bar{\mathbf{H}}$. Assuming $\bar{\bar{\mathbf{H}}}$ is the normalized version of $\bar{\mathbf{X}}$ and $\bar{\mathbf{A}}$ is the diagonal scaling matrix, we obtain:

$$\bar{\bar{\mathbf{X}}} = \bar{\mathbf{A}}\bar{\mathbf{X}} = \bar{\mathbf{A}}\mathbf{H}\hat{\mathbf{S}} = \bar{\bar{\mathbf{H}}}\hat{\mathbf{S}}. \quad (35)$$

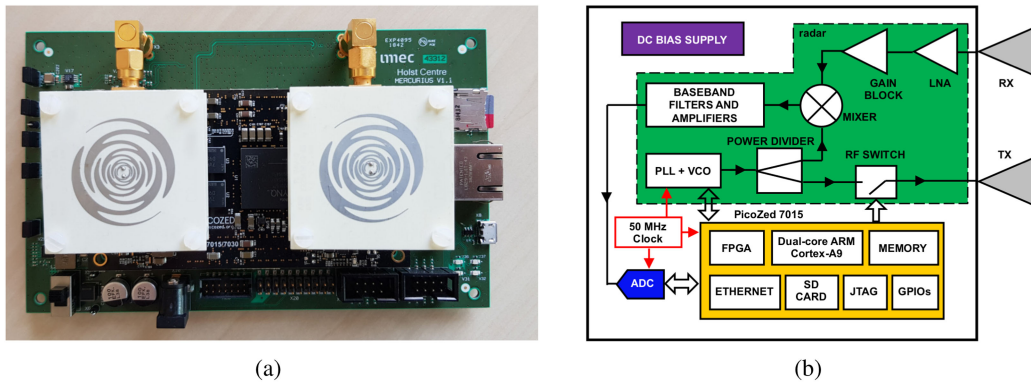


Fig. 4. Radar sensor. (a) Fully assembled radar sensor with antenna pair and (b) block diagram.

We can take the sparsity of the multipath propagation channel into account by adding a suitable constraint to the cost function, i.e., we solve

$$\min_{\hat{\mathbf{H}}} \|\bar{\mathbf{X}} - \mathbf{H}\hat{\mathbf{S}}\|_2^2 + \zeta \|\hat{\mathbf{H}}\|_1, \quad (36)$$

where ζ is the penalty coefficient which represents a trade-off between the residual error and the sparsity. Its value was determined empirically. As the scaling matrix $\bar{\mathbf{A}}$ is known, we obtain

$$\hat{\mathbf{H}} = \bar{\mathbf{A}}\hat{\mathbf{H}}. \quad (37)$$

IV. RADAR SENSOR

In this work, we used the imec Mercurius V1.1 radar sensor (Fig. 4 a) consisting of a custom-designed radar unit and of the PicoZed 7015 system-on-module (SOM) with an integrated field programmable gate array (FPGA). Two commercial sinuous style antennas, with gain of 6 dBi and opening angles of 65 (vertical) \times 85 (horizontal) degrees, are connected to the radar. The latter was developed on a single printed circuit board with a size of approximately 15 (l) \times 9 (w) \times 0.2 (t) cm^3 .

The block diagram of the radar system is shown in Fig. 4 b. The radar's core is formed by the FMCW signal generator, implemented by the HMC703LP4E Fractional-N phase-locked loop (PLL) and by the HMC508LP5 voltage-controlled oscillator (VCO). The FMCW signal is split in two branches by a power divider designed as a branch line coupler. The first output feeds the transmitter antenna through the ADRF5020RF radio-frequency (RF) switch that is controlled by the FPGA to transmit the FMCW signal each T_s . The second output is connected to the MCA1-12G+ mixer's local oscillator (LO) port. The signal reflected from the target (or, more general, from multiple targets) is received, amplified by the HMC902LP3E low-noise amplifier (LNA) and the HMC3587LP3BE gain block, and then mixed with a copy of the transmitting signal (from the second output of the power divider). The resulting baseband signal is bandpass filtered, amplified, and then acquired and digitized by an ADC. The total power consumption is about 8 W.

The radar transmits a series of chirps of initial frequency $f_0 = 7.3$ GHz, total bandwidth $B = 750$ MHz, total duration $T = 102.4\mu\text{s}$ and $T_s = 3.072$ ms. This results in range bins of 20 cm and in a Doppler (vital signs) signal sampling rate

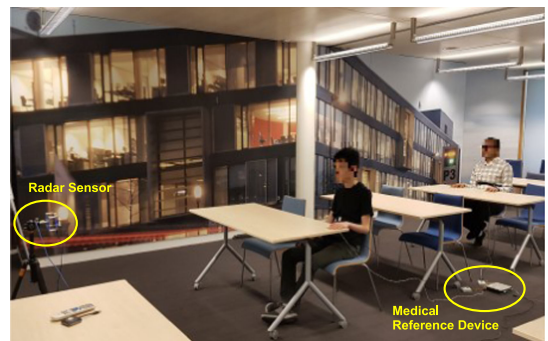


Fig. 5. Experimental environment mimicking an educational class setting. In the figure, the two volunteers are respectively at about 2 m and about 5 m distance from the radar. A medical reference device was used to measure the heartbeat (through PPG sensors with finger transducers) and respiration (through belt sensors) of the volunteers.

of $1/T_s = 325.52$ Hz. The effective radiated peak power is 0dBm. The waveform configuration together with the transmitting power allows satisfying the limits of all the worldwide UWB indoor radio regulations in terms of both power spectral density (-41.3dBmperMHz) and peak power ($0\text{dBm}/50\text{MHz}$) [52].

In case of vital signs with typical speed motion of few millimeters per second, during the T interval there is only a variation of few hundreds of nanoseconds on 20 cm of range resolution. This variation of about 6 orders of magnitude below the range resolution is negligible and cannot result in range/Doppler ambiguity issues. There is also no issue with “long delay return”: the designed radar waveform permits a maximum unambiguous range of several kilometers, while radar-based vital signs monitoring is limited to “room distances”. This is because the electromagnetic signals are strongly attenuated after few meters.

V. EXPERIMENTAL RESULTS

The experimental protocol was approved by the internal imec - Netherlands Ethical Board. In order to generate multipaths that can be experienced in real circumstances, the measurements were performed in a room environment set up as a typical academic class, containing chairs and desks, which are placed near, in front, and behind the volunteers (Figs. 3b,5). This represents a severe multipath situation (as shown in Fig. 3 a) that

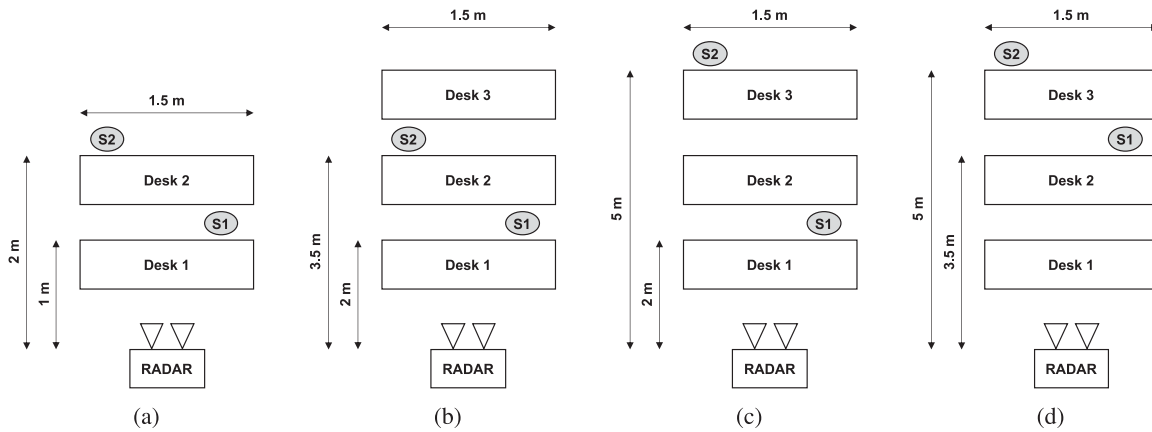


Fig. 6. Sketch of the in-vivo experiments. Scenario of (a) subset 1, (b) subset 2, (c) subset 3 and (d) subset 4. S1 and S2 indicate respectively Subject 1 and Subject 2.

can be experienced in real circumstances: wide and big, partly metal static objects are right in front of the subjects, causing a considerable spreading of the transmitted and reflected signals in the whole room, which has a steel-reinforced concrete floor, metal wall parts and a metal tile ceiling. The validation was conducted with 11 subjects, 9 males and 2 females, differing in height (155-195 cm), in weight, and in age (20 - 34 years). The volunteers were grouped in random pairs and they randomly chose a seat. We performed a total of 21 measurements, subdivided in 4 subsets: (1) 12 experiments with 6 pairs (i.e., 2 measurements per pair) with the subjects at about 1 m and about 2 m distance from the radar; (2) 3 experiments with 3 different pairs (i.e., 1 measurement per pair) with the subjects at about 2 m and about 3.5 m distance from the radar; (3) 3 experiments with 3 different pairs (i.e., 1 measurement per pair) with the subjects at about 2 m and about 5 m distance from the radar; (4) 3 experiments with 3 different pairs (i.e., 1 measurement per pair) with the subjects at about 3.5 m and about 5 m distance from the radar. The aforementioned nominal absolute distances (i.e., 1 m, 2 m, 3.5 m, and 5 m) were measured along the radar's line of sight (LoS), from the antennas to the edges of the tables in front of the subjects. A sketch of the in-vivo experiments is shown in Fig. 6. During the experiments, each subject was breathing normally wearing a photoplethysmogram (PPG) finger sensor and a thorax expansion belt to provide reference measurements for heartbeat and respiration, respectively. At this purpose, we used the g.USBamp device (CE certified and FDA cleared medical device, safety class: II, conformity class: IIa, type of applied part: CF) as gold standard reference. A measuring tape was used to determine the absolute distances between the radar (i.e., from the middle of the two antennas) and the chest surface of the subjects. We have compared the proposed algorithm with the automatic target localization approach based on std [35], [37] where the two highest peaks in the std profile indicated the range bins (i.e., the absolute distances) where the subjects are 1-D located (as explained for Fig. 3 d) and the Doppler signals, extracted from those range bins, were processed using both the linear and arctangent demodulation algorithms. We also processed the data with those two demodulation techniques after extracting the Doppler information from the range bins corresponding to

the tape-measured absolute distances, i.e., performing a manual 1-D localization. Although, in real situations, manual localization obviously cannot be used, we included it in this work as comparison to our algorithm. Obviously, in the benchmarking cases with std and manual localization, we assumed to know a priori the number of subjects. For sake of completeness, we have also validated the proposed algorithm where we replaced the linear demodulation with the arctangent demodulation.

The results of this validation are shown in Figs. 7–10. Each measurement is 140-second long and it was processed considering sliding windows of 20 seconds with overlaps of 19 seconds. Data processing was performed offline using Matlab. The radar data, containing the FFT results of consecutive beat signals, is arranged into a $X(k,m)$ matrix of $L = 30$ rows (i.e., equals to the number of considered range bins) and $M = 45573$ columns (i.e., 140 seconds of signal with $1/T_s$ as sampling frequency in slow time). With 21 measurements, each simultaneously capturing 2 subjects, while applying a latency of 20 seconds, 5040 estimations were performed. For each measurement, we first calculate the target existence probability over 120 sliding windows. The number of subjects is determined looking for the most recurring estimation (i.e., the mode). This value is then used for the vital signs monitoring and automatic localization tasks. Figs. 7a,8a,9a,10a shows the average target existence probability for the four subsets. For the vital signs, we determined the detection success rate as the percentage of time that the estimated respiration rate (RR) and heart rate (HR) and their references match respectively within 1.5 breaths-per-minute and 3 heartbeats-per-minute. These thresholds are below the maximum errors to consider the measurements clinically acceptable [47]. For the 1-D localization, we calculated the mean absolute errors (MAEs) and the RMS errors (RMSEs). With this dataset, we experienced that the approaches exploiting the linear demodulation technique outperform the alternative ones where the arctangent demodulation was used. Anyhow, we reported higher vital signs success rates when the arctangent demodulation was employed in combination with the proposed algorithm rather than with the std-based and manual localization alternatives. The rest of the following discussion focuses only on the approaches using the linear demodulation. For all the

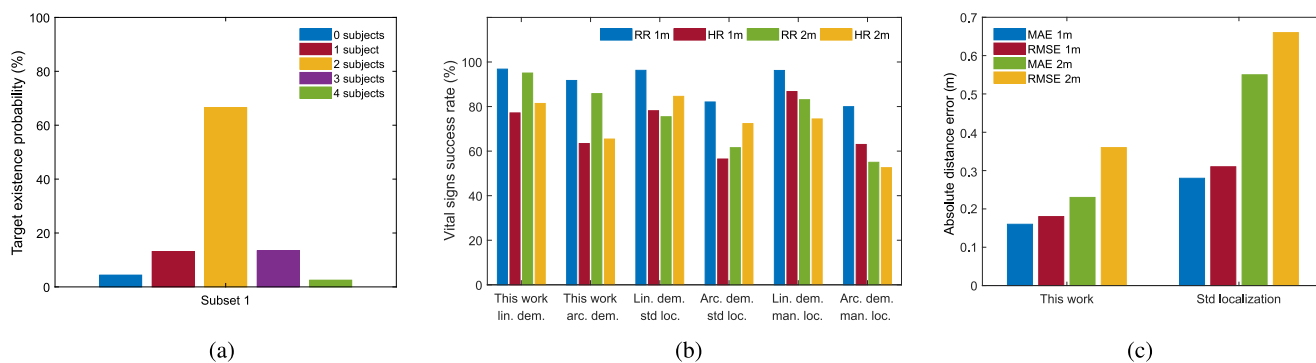


Fig. 7. Experimental results with the subjects seated at 1 m and 2 m distance from the radar sensor (subset 1) and comparison of the proposed algorithm with some of the state-of-the-art approaches. (a) Target existence probability. (b) vital signs monitoring, (c) automatic 1-D localization.

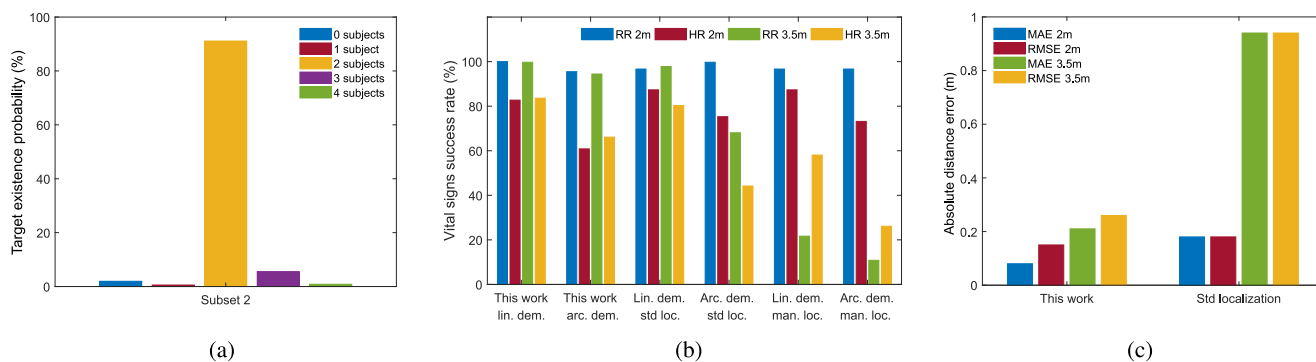


Fig. 8. Experimental results with the subjects seated at 2 m and 3.5 m distance from the radar sensor (subset 2) and comparison of the proposed algorithm with some of the state-of-the-art approaches. (a) Target existence probability. (b) vital signs monitoring, (c) automatic 1-D localization.

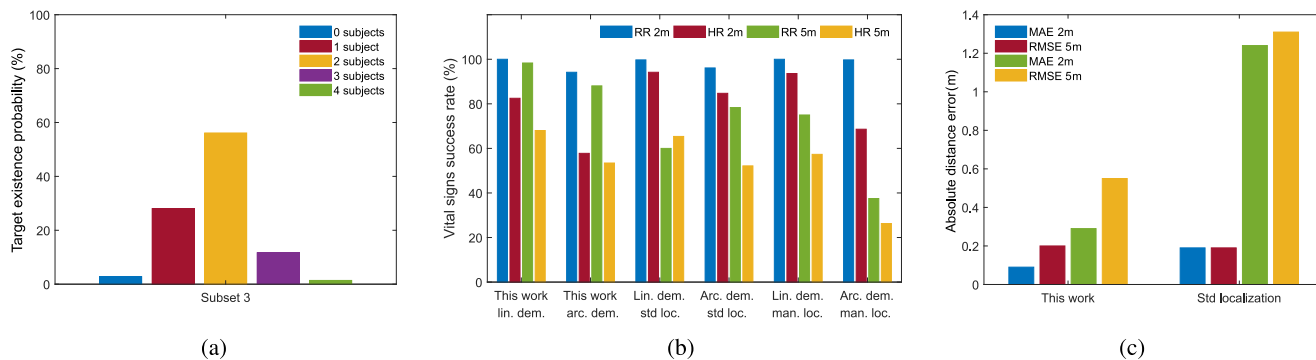


Fig. 9. Experimental results with the subjects seated at 2 m and 5 m distance from the radar sensor (subset 3) and comparison of the proposed algorithm with some of the state-of-the-art approaches. (a) Target existence probability. (b) vital signs monitoring, (c) automatic 1-D localization.

subsets, we obtained similar respiration success rates for the first targets (almost 100%), although the linear demodulation algorithm with manual localization gives a higher success rate in estimating the heart rates. This is expected, because: (1) the nearest subjects (and thus the corresponding range bins) are not influenced by the multipaths and, therefore, they can be considered independent from further away subjects; (2) the std-based localization algorithm and, in particular, the proposed methodology consider during the processing all the range bins at the same time (therefore also the ones affected by multipath) while the manual localization considers only the range bin where the first target is present. However, we obtain better results

over the std-based approach in the 1-D localization of the first subjects. In fact, as opposed to the std-based alternative, with the proposed algorithm the errors are within the radar range resolution of 20 cm. The real benefit of the proposed algorithm is experienced in monitoring the second subjects which are affected by the multipaths. In fact, not only does our algorithm produce higher overall success rates than the other two approaches in estimating the vital signs rates (both for RR and HR), but it also considerably outperforms the std-based localization algorithm both in terms of MAEs and of RMSEs. In fact, with the proposed methodology, the errors are very close to the radar range resolution while, with the other approaches, they are

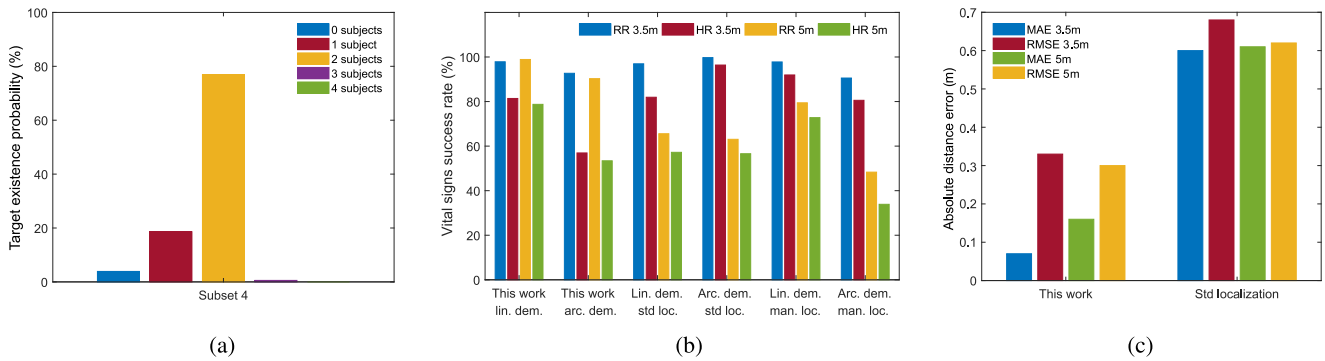


Fig. 10. Experimental results with the subjects seated at 3.5 m and 5 m distance from the radar sensor (subset 4) and comparison of the proposed algorithm with some of the state-of-the-art approaches. (a) Target existence probability. (b) vital signs monitoring, (c) automatic 1-D localization.

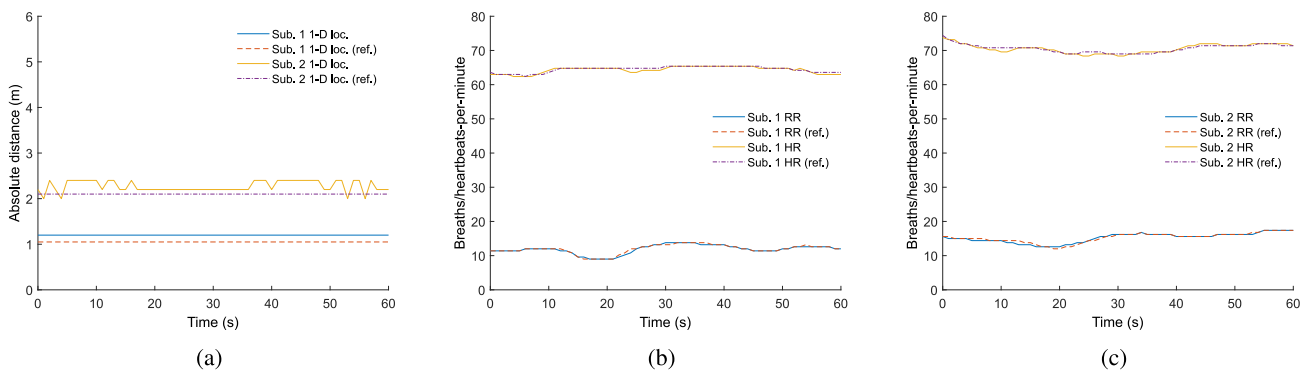


Fig. 11. Experimental results with two subjects at about 1 m and about 2 m distance from the radar. The volunteers were seated and facing the radar. (a) 1-D localization. (b) Vital signs rates over time of Subject 1. (c) Vital signs rates over time of Subject 2.

always significant (even beyond 1.2 m). In a few measurements (Fig. 8 b), the std-based localization with linear demodulation produced comparable results (although slightly minor success rates) to our algorithm in the vital signs estimation of the second target, although the benchmarking solution produces a significant error in the 1-D localization (Fig. 8 c). This happens when the std profile produces a peak to a range bin where it is present a multipath of the second target (i.e., a copy) which luckily is not affected by the multipath of the first person. This concept was demonstrated with the help of Fig. 3 d.

Finally, Fig. 11 shows the results of an experiment with two seated down subjects respectively at about 1 m and about 2 m distance from the radar. More precisely, Fig. 11 a shows the result of the 1-D localization over time while Figs. 11b,c show the vital signs rates over time of the two subjects. This example demonstrates that the proposed algorithm does not require distinct breathing rates for a proper monitoring.

VI. CONCLUSION

We report an algorithm based on an FMCW radar sensor that can automatically determine the absolute distances (1-D localization) of paired subjects and remotely monitor their vital signs. The proposed methodology differentiates from current state-of-the-art approaches and it is demonstrated to function in real indoor environments where radar signals are severely affected by multipaths. Practical applications arise for health

care, assisted living, geriatric and quarantine medicine, rescue and security purposes. Further research should now aim to implement this method using real-time embedded signal processing and to extend the algorithm towards a multiple-input and multiple-output (MIMO) system in order to enable 2-D localization (range and azimuth information). This allows monitoring subjects that are at the same absolute distance (range bin) but at different angular locations. Moreover, as opposite to SISO, a MIMO radar divides the whole environment in “azimuth-range cells”. Each cell has an area smaller than the one of the entire range bin, thus is affected by a minor amount of multipath reflections. Although this work was based on an FMCW radar, the proposed methodology can be applied to any other UWB architecture (e.g., FMCW, SFCW, PMCW and UWB-IR). The direct path and multipath reflections combine following the same physic principles independently from the radar type. The resulting demodulated signals are mathematically expressed as complex exponential functions, therefore they follow the same theory described in this manuscript.

REFERENCES

- [1] O. Boric-Lubeke and V. M. Lubecke, “Wireless house calls: Using communications technology for health care and monitoring,” *IEEE Microw. Mag.*, vol. 3, no. 3, pp. 43–48, Sep. 2002.
- [2] I. Korhonen, J. Parkka and M. Van Gils, “Health monitoring in the home of the future,” *IEEE Eng. Med. Biol. Mag.*, vol. 22, no. 3, pp. 66–73, Jul. 2003.
- [3] C. Li, *et al.*, “Radar remote monitoring of vital signs,” *IEEE Microw. Mag.*, vol. 10, no. 1, pp. 47–56, Jan. 2009.

- [4] D. Schreurs, and M. Mercuri, "Contactless medical sensing," in *Proc. IEEE MTT-S Int. Microw. Symp. Dig.*, 2015, pp. 1–4.
- [5] E. Schires, P. Georgiou and T. S. Lande, "Vital sign monitoring through the back using an UWB impulse radar with body coupled antennas," *IEEE Trans. Biomed. Circuits Syst.*, vol. 12, no. 2, pp. 292–302, Apr. 2018.
- [6] I. D. Castro, *et al.*, "Physiological driver monitoring using capacitively coupled and radar sensors," *Appl. Sci.*, vol. 9, no. 19, pp. 1–15, Sep. 2019.
- [7] F. Wang, *et al.*, "Detection of concealed individuals based on their vital signs by using a see-through-wall imaging system with a self-injection-locked radar," *IEEE Trans. Microw. Theory Techn.*, vol. 61, no. 1, pp. 696–704, Jan. 2013.
- [8] X. Liang, *et al.*, "Ultra-wideband impulse radar through-wall detection of vital signs," *Sci. Rep.*, vol. 8, no. 13367, pp. 1–21, Sep. 2018.
- [9] Z. Chen, *et al.*, "Study on the multipath propagation characteristics of UWB signal for indoor lab environments," in *Proc. IEEE Int. Conf. Ubiquitous Wireless Broadband*, 2016, pp. 1–4.
- [10] Y. Yoon, J. Kim and Y. Chong, "Multipath delay characteristic in mm-wave radio propagation in indoor public area," in *Proc. Int. Conf. Inf. Commun. Technol. Convergence*, 2016, pp. 966–968.
- [11] Q. H. Spencer, *et al.*, "Modeling the statistical time and angle of arrival characteristics of an indoor multipath channel," *IEEE J. Sel. Areas Commun.*, vol. 18, no. 2, pp. 347–360, Mar. 2000.
- [12] C. Li and J. Lin, "Random body movement cancellation in doppler radar vital sign detection," *IEEE Trans. Microw. Theory Techn.*, vol. 56, no. 12, pp. 3143–3152, Dec. 2008.
- [13] B. K. Park, O. Boric-Lubecke, and V. M. Lubecke, "Arctangent demodulation with DC offset compensation in quadrature doppler radar receiver systems," *IEEE Trans. Microw. Theory Techn.*, vol. 55, no. 5, pp. 1073–1079, May 2007.
- [14] I. Mostafanezhad, E. Yavari and O. Boric-Lubecke, "A low cost simple RF front end using time-domain multiplexing for direction of arrival estimation of physiological signals," in *Proc. IEEE MTT-S Int. Microw. Symp. Dig.*, 2013, pp. 1–4.
- [15] M. Mercuri, D. Schreurs and P. Leroux, "Optimised waveform design for radar sensor aimed at contactless health monitoring," *Electron. Lett.*, vol. 48, no. 20, pp. 1255–1257, Sep. 2018.
- [16] C. Gu *et al.*, "Accurate respiration measurement using DC-Coupled continuous-wave radar sensor for motion-adaptive cancer radiotherapy," *IEEE Trans. Biomed. Eng.*, vol. 59, no. 11, pp. 3117–3123, Nov. 2012.
- [17] D. Buxi, *et al.*, "Systolic time interval estimation using continuous wave radar with on-body antennas," *IEEE J. Biomed. Health Inform.*, vol. 22, no. 1, pp. 129–139, Jul. 2017.
- [18] F. K. Wang *et al.*, "A novel vital-sign sensor based on a self-injection-locked oscillator," *IEEE Trans. Microw. Theory Technol.*, vol. 58, no. 12, pp. 4112–4120, Dec. 2010.
- [19] F. K. Wang, *et al.*, "Single-antenna doppler radars using self and mutual injection locking for vital sign detection with random body movement cancellation," *IEEE Trans. Microw. Theory Technol.*, vol. 59, no. 12, pp. 3577–3587, Dec. 2011.
- [20] M. Tang, F. Wang and T. Horng, "Single self-injection-locked radar with two antennas for monitoring vital signs with large body movement cancellation," *IEEE Trans. Microw. Theory Technol.*, vol. 65, no. 12, pp. 5324–5333, Dec. 2017.
- [21] M. Mercuri, *et al.*, "Frequency-tracking CW doppler radar solving small-angle approximation and null point issues in non-contact vital signs monitoring," *IEEE Trans. Biomed. Circuits Syst.*, vol. 11, no. 3, pp. 671–680, Jun. 2017.
- [22] M. Mercuri *et al.*, "A direct phase-tracking doppler radar using wavelet independent component analysis for non-contact respiratory and heart rate monitoring," *IEEE Trans. Biomed. Circuits Syst.*, vol. 12, no. 3, pp. 632–643, Apr. 2018.
- [23] A. Bin-Obadi, *et al.*, "A survey on vital signs detection using radar techniques and processing with FPGA implementation," *IEEE Circuits Syst. Mag.*, vol. 21, no. 1, pp. 41–74, Firstquarter 2021.
- [24] W. Su, *et al.*, "Stepped-frequency continuous-wave radar with self-injection-locking technology for monitoring multiple human vital signs," *IEEE Trans. Microw. Theory Technol.*, vol. 67, no. 12, pp. 5396–5405, Dec. 2019.
- [25] G. Sacco, *et al.*, "A radar system for indoor human localization and breath monitoring," in *Proc. IEEE Int. Symp. Med. Meas. Appl.*, 2018, pp. 1–6.
- [26] G. Sacco, *et al.*, "An FMCW radar for localization and vital signs measurement for different chest orientations," *Sensors*, vol. 20, no. 12, pp. 1–14, Jun. 2020.
- [27] G. Wang, *et al.*, "Application of linear-frequency-modulated continuous-wave (LFMCW) radars for tracking of vital signs," *IEEE Trans. Microw. Theory Techn.*, vol. 62, no. 6, pp. 1387–1399, Jun. 2014.
- [28] M. Mercuri, *et al.*, "Digital linear discrete FMCW radar for healthcare applications," in *Proc. IEEE MTT-S Int. Microw. Symp. Dig.*, 2019, pp. 144–147.
- [29] Liu *et al.*, "9.3 A680 μ W burst-chirp UWB radar transceiver for vital signs and occupancy sensing up to 15 m distance," in *Proc. IEEE ISSCC Dig. Tech. Papers*, Feb. 2019, pp. 166–167.
- [30] Y. Liu, *et al.*, "An ultralow power burst-chirp UWB radar transceiver for indoor vital signs and occupancy sensing in 40-nm CMOS," *IEEE Solid-State Circuits Lett.*, vol. 2, no. 11, pp. 256–259, Nov. 2019.
- [31] M. Mercuri, *et al.*, "Vital-sign monitoring and spatial tracking of multiple people using a contactless radar-based sensor," *Nat. Electron.*, vol. 2, pp. 252–262, Jun. 2019.
- [32] J. Wang, *et al.*, "A spectrum-efficient FSK radar technology for range tracking of both moving and stationary human subjects," *IEEE Trans. Microw. Theory Techn.*, vol. 67, no. 12, pp. 5406–5416, Dec. 2019.
- [33] T. Sakamoto *et al.*, "Feature-based correlation and topological similarity for interbeat interval estimation using ultrawideband radar," *IEEE Trans. Biomed. Eng.*, vol. 63, no. 4, pp. 747–757, Apr. 2016.
- [34] Z. Peng *et al.*, "A portable FMCW interferometry radar with programmable Low-IF architecture for localization, ISAR imaging, and vital sign tracking," *IEEE Trans. Microw. Theory Technol.*, vol. 65, no. 4, pp. 1334–1344, Apr. 2017.
- [35] G. Wang, *et al.*, "A hybrid FMCW-Interferometry radar for indoor precise positioning and versatile life activity monitoring," *IEEE Trans. Microw. Theory Technol.*, vol. 62, no. 11, pp. 2812–2822, Nov. 2014.
- [36] F. Adib, *et al.*, "Smart homes that monitor breathing and heart rate," in *Proc. 33rd Annu. ACM Conf. Hum. Factors Comput. Syst.*, 2015, pp. 837–846.
- [37] F. Adib, Z. Kabelac and D. Katabi, "Multi-person localization via RF body reflections," in *Proc. 12th USENIX Conf. Networked Syst. Des. Implementation*, 2015, pp. 279–292.
- [38] S. Wang *et al.*, "A novel ultra-wideband 80 GHz FMCW radar system for contactless monitoring of vital signs," in *Proc. IEEE 37th Annu. Int. Conf. Eng. Med. Biol. Soc.*, 2015, pp. 4978–4981.
- [39] F. Wang, *et al.*, "ViMo: Multi-person vital sign monitoring using commodity millimeter wave radio," *IEEE Int. Things J.*, vol. 8, no. 3, pp. 1294–1307, Feb. 2021.
- [40] M. Longbrake, "True time-delay beamsteering for radar," in *Proc. IEEE Nat. Aerosp. Electron. Conf.*, 2012, pp. 246–249.
- [41] A. Alarifi *et al.*, "Ultra wideband indoor positioning technologies: Analysis and recent advances," *Sensors*, vol. 16, no. 5, pp. 1–36, Mar. 2016.
- [42] F. Wang, *et al.*, "ViMo: Multi-person vital sign monitoring using commodity millimeter wave radio," *IEEE Internet Things J.*, vol. 8, no. 3, pp. 1294–1307, Feb. 2021.
- [43] J. Liu, *et al.*, "Tracking vital signs during sleep leveraging off-the-shelf wifi," in *Proc. 16th ACM Int. Symp. Mobile Ad Hoc Netw. Comput.*, 2015, pp. 267–276.
- [44] Z. Yang, *et al.*, "Monitoring vital signs using millimeter wave," in *Proc. 17th ACM Int. Symp. Mobile Ad Hoc Netw. Comput.*, 2016, pp. 211–220.
- [45] M. Mercuri *et al.*, "2-D localization, angular separation and vital signs monitoring using a SISO FMCW radar for smart long-term health monitoring environments," *IEEE Internet Things J.*, vol. 8, no. 14, pp. 11065–11077, Jul. 15, 2021.
- [46] W. C. Jakes and D. C. Cox, *Microwave Mobile Communications*, Hoboken, NJ, USA: Wiley-IEEE Press, 1994.
- [47] M. Weenk, *et al.*, "A smart all-in-one device to measure vital signs in admitted patients," *PLoS One*, vol. 13, pp. 1–12, Feb. 2018.
- [48] V. D. Vrabie and J. I. Mars, "SVD-ICA: A. new tool to enhance the separation between signal and noise subspaces," in *Proc. 11th Eur. Signal Process. Conf.*, 2002, pp. 1–4.
- [49] G. D. Clifford, "Singular value decomposition and independent component analysis for blind signal separation," *Bio. Signal Image Process.*, vol. 44, pp. 1–49, Apr. 2005. [Online]. Available: https://www.academia.edu/15156422/HST582J_6_555J_16_456J_Biomedical_Signal_and_Image_Processing_Spring_2005_Singular_Value_Decomposition_and_Independent_Component_Analysis_for_Blind_Source_Separation
- [50] Y. Unnisa, D. Tran and F. Huang, "Statistical independence, measures and testing," in *Proc. APCOM ISCM*, Dec. 2013, pp. 1–8.
- [51] M. Novey and T. Adali, "Complex ICA by negentropy maximization," *IEEE Trans. Neural Netw.*, vol. 19, no. 4, pp. 596–609, Apr. 2018.
- [52] H. W. Pflug *et al.*, "Method to estimate impulse-radio ultra-wideband peak power," *IEEE Trans. Microw. Theory Technol.*, vol. 59, no. 4, pp. 1174–1186, Apr. 2011.